Improving OCTA Imaging through Cross-Domain Adaptation: A Noise-Guided Framework Using Intralipid-Enhanced Rat Data

Bingyu Yang[1,2], Bingyao Tan[3,4], Zaiwang Gu[2], Leopold Schmetterer[3,4], Huiqi Li[1](✉), and Jun Cheng[2](✉)

[1] Beijing Institute of Technology, Beijing, China
`huiqili@bit.edu.cn`
[2] Institute for Infocomm Research, Agency for Science, Technology and Research (A*STAR), Singapore, Singapore
`cheng_jun@i2r.a-star.edu.sg`
[3] Singapore Eye Research Institute, Singapore National Eye Center, Singapore, Singapore
[4] Duke-NUS Medical School, Singapore, Singapore

Abstract. Deep learning has been introduced into optical coherence tomography angiography (OCTA) imaging, which is a non-invasive technique for visualizing vascular structures. Intralipid injection has shown promise in improving blood cell scattering for better OCTA imaging. However, administering intralipid to human subjects for imaging purposes may raise ethical concerns. To address this challenge, we acquire intralipid-enhanced OCTA in rats and introduce cross-domain learning to address the domain shifts. Specifically, we collect data from eyes of anesthetized rats to obtain motion-free data and introduce a noise-guided self-training framework to bridge the domain gaps between rats and primates. Additionally, an en face enhancement loss is incorporated to further refine en face vectors during adaptation. Compared with other classical and fully supervised OCTA imaging algorithms, our method improves B-scan denoising performance by 53.1% and 65.0% on CNR and BRISQUE in human subjects respectively, while enhancing vessel contrast in en face images.

Keywords: OCTA · Image enhancement · Domain adaptation · Self-training

1 Introduction

Optical coherence tomography angiography (OCTA) is a noninvasive technique that provides a three-dimensional visualization of the retina and choroid vasculature [15]. It uses red blood cell motion as a natural agent to detect blood flow, capturing signal differences between repeated OCT B-scans at the same position [24]. This non-invasive method offers advantages over dye-based techniques including fluorescein angiography and indocyanine green angiography [13]. With advantages in imaging speed and non-invasiveness, OCTA serves as an effective tool in clinical diagnosis [5] and computer-aided algorithms [31],[33].

OCTA imaging algorithms have recently attracted considerable research interest for diagnosis and detection [6]. Despite significant advances in motion artifact correction, OCTA denoising remains a key challenge [3]. Classical OCTA imaging methods include phase-signal-based, intensity-signal-based, and complex-signal-based algorithms [18]. Representative algorithms, such as optical microangiography (OMAG) [29], reduce noise based on the repeated OCT B-scans.

For deep learning methods, innovations primarily focus on model inputs and ground truth generation. For example, Liu *et al.* [19] proposed to obtain ground truth using a classical OCTA imaging algorithm from 48 repeated scans at the same slow-axis position. Similarly, adjacent OCT B-scans are also leveraged in [4], [12] and [17] to reduce noise in fully or weakly supervised learning. Moreover, Jiang *et al.* [11] proposed an OCTA denoising method inspired by Noise2Noise [14], where repeated B-scans at the same position are split for input and ground truth, respectively. For these deep learning methods, U-Net, transformers [20] and generative adversarial networks (GANs) are commonly utilized [16], with both two-dimensional (2D) and three-dimensional (3D) neural networks being explored [12]. While these methods show the feasibility of deep learning based OCTA, they rely on a large number of repeated scans from human subjects to obtain ground truth, which suffer from motion artifacts.

Besides overlapping scanning, intralipid injection is another approach to improve OCTA imaging as it improves the scattering of the blood cells [1]. However, it is ethnically infeasible to apply to human subjects due to safety concerns as it may interact with ocular tissues unpredictably. In this paper, we propose to apply intralipid injection and collect data from the eyes of anesthetized rats to obtain high-quality ground truth with minimum motion. As there are domain gaps between rats and primates, we propose cross-domain learning for OCTA imaging. The contributions are as follows:

- We propose using data from intralipid rats and a source-free self-training framework for cross-domain OCTA imaging. The self-training framework incorporates noise estimation for adaptive denoising, mitigating domain gaps effectively.
- We propose an en face enhancement loss to improve the OCTA en face contrast during B-scan denoising.
- Our method achieves better quantitative scores and visual evaluation than the state-of-the-art methods across multiple OCTA datasets.

2 Method

2.1 Preliminary – Source Domain Imaging

Our approach first trains an OCTA imaging model in the source domain, then adapts and improves it in the target domain. For the source domain, denote OCT or OCTA volumes as $\{X^s, Y^s\}$, where $X^s \in \mathbb{R}^{H^s \times W^s \times M^s \times N^s}$ represents OCT

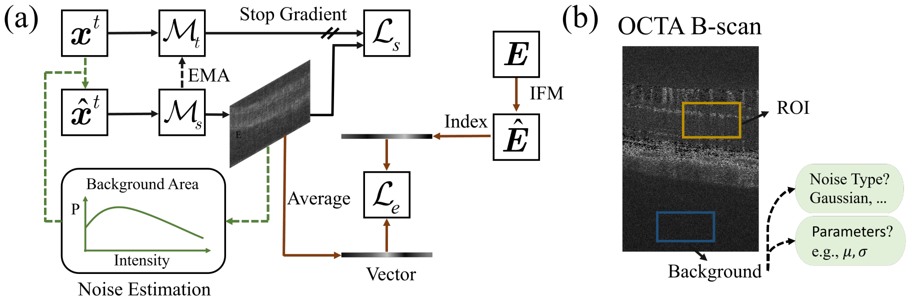

Fig. 1: Flowchart of the target domain adaptation. (a) The proposed self-training framework. The teacher network is used to guide the student network in a self-supervised manner, while en face is enhanced. (b) Noise estimation of OCTA.

B-scan volumes with height H^s, width W^s, repeated frames per position M^s and the number of slow-axis positions N^s. And $Y^s \in \mathbb{R}^{H^s \times W^s \times 1 \times N^s}$ is OCTA ground truth. Similar to other deep learning methods, we utilize classical OCTA algorithms to generate pseudo ground truth for the source domain.

We first improve the classical OMAG [29] algorithm by leveraging adjacent positions for ground truth generation inspired by [12], [17]. Denote $\boldsymbol{x}^s_{m,n}$ as the OCT B-scans at frame m and position n, and denote $\boldsymbol{y}^s_n$ as the corresponding OCTA B-scan image, the improved OMAG is expressed as:

$$\boldsymbol{y}^s_n = \frac{1}{(2k+1) \times (M^s - 1)} \sum_{j=n-k}^{n+k} \sum_{i=1}^{M^s-1} \left| \boldsymbol{x}^s_{i,j} - \boldsymbol{x}^s_{i+1,j} \right|, \qquad (1)$$

where k represents the number of adjacent positions. The adjacent OCT B-scans are registered [7] before ground truth generation. We utilize L_1 loss for training after obtaining the ground truth. After training, the model acquires the capability of OCTA construction and its denoising ability is improved, as the ground truth Y^s is obtained using adjacent positions.

2.2 Target Domain Self-Training with Noise Estimation

Distribution shifts, such as variations in noise intensity across datasets, often lead to significant performance decline for pre-trained models, presenting a significant challenge for deep-learning OCTA imaging methods [10]. Therefore, we design a self-supervised framework for target domain OCTA adaptation, which is shown in Fig. 1. The framework comprises a student network $\mathcal{M}_s$ and a teacher network $\mathcal{M}_t$, both of which share the same architecture as the source domain for weight transfer. They are initialized with the weights trained in the source domain (i.e., intralipid rats), and the teacher network is updated as the exponential moving average (EMA) [2] of the student network. The outputs of the teacher network are used as the pseudo ground truth to guide and constrain the student network.

During self-training processes for segmentation or classification, many methods apply weak augmentation and strong augmentation for teacher networks and student networks, respectively [25]. For OCTA adaptation, various noise is added to the input of the student network to address domain gaps and enhance the model's denoising capability. In contrast, the teacher network directly takes the original OCT images as input without augmentation, ensuring the pseudo ground truth with minimal noise. The target domain data is denoted as X^t, where $\boldsymbol{x}^t \in \mathbb{R}^{H^t \times W^t \times M^t \times 1}$ represents a single position within it. And the data with added noise is denoted as $\hat{\boldsymbol{x}}^t$. The self-training loss can be represented as:

$$\mathcal{L}_s = \|\mathcal{M}_t(\boldsymbol{x}^t) - \mathcal{M}_s(\hat{\boldsymbol{x}}^t)\|_1, \tag{2}$$

where $\mathcal{M}_t(\boldsymbol{x}^t)$ represents the pseudo ground truth from the teacher network, and the parameters remain fixed during backpropagation.

To introduce appropriate noise to the student network, we estimate noise from its outputs, as shown in Fig. 1(b). In OCTA images, the region of interest (ROI) lies in the choroid and above, containing both signal and noise, while the sclera layer, at the bottom, does not have vascular information [9]. So it serves as the background for noise estimation in our method. We use the Kolmogorov-Smirnov (KS) test [21] to determine the noise type, such as Gaussian, Poisson, or exponential noise. We select the noise type with the smallest maximum deviation D of KS test,

$$D = \max \left| EDF(\hat{\boldsymbol{y}}^t|_b) - CDF(\hat{\boldsymbol{y}}^t|_b) \right|, \tag{3}$$

where $EDF(\cdot)$ and $CDF(\cdot)$ are Empirical Distribution Function and Cumulative Distribution Function respectively. $\hat{\boldsymbol{y}}^t|_b$ is the background area from $\hat{\boldsymbol{y}}^t$, and $\hat{\boldsymbol{y}}^t = \mathcal{M}_s(\hat{\boldsymbol{x}}^t)$. Then, the parameters are estimated through maximum likelihood estimation (MLE) [23]. After fitting the noise parameters, we sample and add noise to the input $\boldsymbol{x}^t$. A sliding average stabilizes the noise parameters during training. These parameters also indicate training progress. A low level of estimated noise indicates that the denoising process is sufficient, allowing early stopping to prevent overfitting.

2.3 En Face Constraints for Enhancement

En face images play a critical role in clinical diagnosis. Therefore, it is necessary to not only denoise OCTA B-scan but also enhance en face images [28]. En face images $\boldsymbol{E} \in \mathbb{R}^{W^t \times N^t}$ is usually obtained by averaging the OCTA B-scans along the axial direction and then stacking them, where W^t and N^t are the width and the number of positions respectively. And the OCTA B-scans for en face can be generated using either the pre-trained model or classical methods.

Image formation model (IFM) [8] is a classical approach that is widely used in natural image dehazing and image enhancement [32]. Our method applies IFM to enhance en face images. The equation is expressed as:

$$\hat{\boldsymbol{E}} = \frac{\boldsymbol{E} - \boldsymbol{A}}{\boldsymbol{t}} + \boldsymbol{A}, \tag{4}$$

Table 1: Datasets.

Object	Domain	Intralipid	OCTA Images		Volumes	Data Size
Rat	Source	✓	14308	(Train)	28	$512 \times 1024 \times 4 \times 511$
Monkey	Target	✗	1500/1500	(Adapt/Test)	1/1	$1024 \times 1536 \times 3 \times 1500$
Human	Target	✗	2025/225	(Adapt/Test)	9/1	$256 \times 992 \times 3 \times 225$

where $\boldsymbol{A}$ represents the global atmospheric light in IFM, which can be estimated by the local average of the brightness of the original en face image $\boldsymbol{E}$ in our method. And $0 < \boldsymbol{t} \leq 1$ describes the transmissivity of the medium. The enhanced en face $\hat{\boldsymbol{E}}$ can be obtained given the transmission parameter $\boldsymbol{t}$.

Subsequently, the enhanced en face $\hat{\boldsymbol{E}} = [\hat{\boldsymbol{e}}_1; \hat{\boldsymbol{e}}_2; \ldots; \hat{\boldsymbol{e}}_{N^t}]$ is employed to constrain the student network, where each lateral vector $\hat{\boldsymbol{e}}$ represents a single slow-axis position. During the training process, the output of the student network $\hat{\boldsymbol{y}}^t$ is averaged along the axis to obtain a lateral en face vector $\boldsymbol{z}$, where $\hat{\boldsymbol{e}}, \boldsymbol{z} \in \mathbb{R}^{1\times W^t}$. In general, images with higher noise intensity tend to have higher mean values in their lateral en face vectors. As denoising reduces noise in non-ROI regions, the mean of lateral en face vectors decreases. Therefore, we utilize the Pearson correlation coefficient to reduce the impact of noise in the label $\hat{\boldsymbol{e}}$. The en face enhancement loss is represented as:

$$\mathcal{L}_e = 1 - r(\hat{\boldsymbol{e}}, \boldsymbol{z}), \tag{5}$$

$$r(\hat{\boldsymbol{e}}, \boldsymbol{z}) = \frac{\sum(\hat{\boldsymbol{e}} - \mu(\hat{\boldsymbol{e}}))(\boldsymbol{z} - \mu(\boldsymbol{z}))}{\sqrt{\sum(\hat{\boldsymbol{e}} - \mu(\hat{\boldsymbol{e}}))^2}\sqrt{\sum(\boldsymbol{z} - \mu(\boldsymbol{z}))^2}}, \tag{6}$$

where $r(\hat{\boldsymbol{e}}, \boldsymbol{z})$ is the Pearson correlation coefficient. $\mu(\cdot)$ is used to calculate the mean of the vector. The overall loss function is expressed as follows:

$$\mathcal{L} = \mathcal{L}_s + \lambda \mathcal{L}_e. \tag{7}$$

After training, the teacher network is saved to serve as the imaging and enhancement model.

3 Experiments

3.1 Experimental Settings

Data collection: We utilize OCTA from rats, monkeys and humans in our study, and the collected data is described in Table 1. We use a Cirrus Angioplex SD-OCT for rat data, capturing 4 frames per slow-axis position across 511 positions, with a size of 512 × 1024 for B-scans. The rats were injected intravenously with 20% intralipid (3ml/kg). The rat OCTA exhibits high quality and low noise levels for OCTA data and therefore is used as the source domain. For the target domain, monkey and human data is collected without intralipid and each position is scanned only three times, resulting in a high noise level

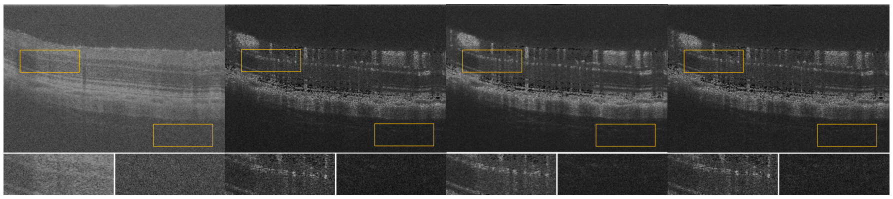

(a) OCTARA [26] (b) OMAG [29] (c) i-OMAG (d) Li *et al.* [16]

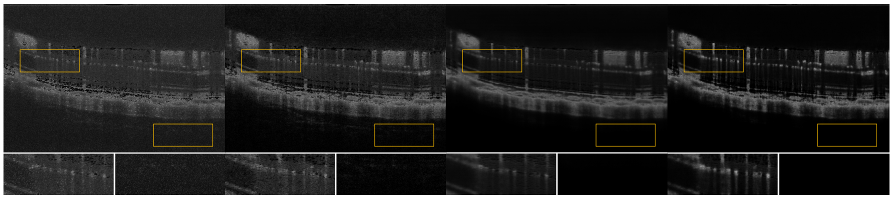

(e) Jiang *et al.* [11] (f) w/o $\mathcal{L}_s$ & $\mathcal{L}_e$ (g) w/o $\mathcal{L}_e$ (h) Ours

Fig. 2: OCTA B-scans of monkey. ROI and background are enlarged below.

for B-scans. In rat and monkey data collection, the subjects were anesthetized with a mixed sedative to prevent motion artifacts. Monkey and human data are adapted separately.

Model training: An U-Net architecture with 8× downsampling is employed as the backbone. For the source domain, we use 3 repeated B-scans as the input and ground truths are generated using OMAG algorithm [29] with 12 frames of OCT B-scans from adjacent locations ($k = 1$). During self-training, an additional fixed noise is introduced as momentum, based on the noise parameters of the early stage, to accelerate the training process. And the momentum of EMA is set to 0.999.

Evaluation: We use no-reference evaluation metrics due to the absence of golden ground truth. For B-scans, contrast-to-noise ratio (CNR) [30] and BRISQUE [22] (BRI) are utilized. The background region for CNR is from the deep sclera region, while the ROI region is above the choroid. For en face, entropy [27] (ENT) is used to evaluate the overall performance. We also compute the intensity difference between vessels and background along line segments, referred to as the vessel contrast score (VC), to evaluate vessel enhancement.

3.2 Ablation Studies

The monkey data is used for our ablation study because it does not have motion artifacts. Quantitative evaluation results are shown in Table 2. The visual comparison of B-scan and en face images is shown in Fig. 2 and Fig. 3, respectively.

B-scan denoising: The baseline (w/o $\mathcal{L}_s$ & $\mathcal{L}_e$) achieves a CNR of 14.8 and a BRISQUE of 45.3 for the target domain (monkey) with the source domain weights (rat). However, it achieves a CNR of 32.9 and a BRISQUE of 30.2 when

Table 2: Ablation study on monkey OCTA.

	B-scan		En face	
	CNR ↑	BRI ↓	ENT ↑	VC ↑
w/o $\mathcal{L}_s$ & $\mathcal{L}_e$	14.8	45.3	4.17	56.8
w/o $\mathcal{L}_e$	27.9	10.9	3.93	78.3
Ours ($\lambda = 0.2$)	28.6	8.4	4.16	85.7
Ours ($\lambda = 5$)	27.5	12.5	**4.22**	85.9
Ours ($\lambda = 1$)	**31.4**	**7.6**	4.21	**87.4**

Table 3: Comparison with other methods.

	Monkey				Human			
	B-scan		En face		B-scan		En face	
	CNR ↑	BRI ↓	ENT ↑	VC ↑	CNR ↑	BRI ↓	ENT ↑	VC ↑
OCTARA [26]	1.2	74.8	4.1	40.8	2.6	25.7	3.2	9.5
OMAG [29]	3.3	80.9	4.0	44.4	2.4	72.7	3.3	9.7
i-OMAG	5.2	63.9	4.1	51.9	9.9	36.6	3.0	10.6
Li *et al.* [16]	2.4	84.9	4.1	41.7	5.2	72.5	3.1	17.2
Jiang *et al.* [11]	6.3	55.5	3.8	39.5	14.5	19.7	2.9	20.3
Ours	**31.4**	**7.6**	**4.2**	**87.4**	**22.2**	**6.9**	**3.6**	**53.2**

tested on the source domain. The performance drop in the target domain is because of a domain gap, such as differences in signal-to-noise ratios and species. There is a significant improvement in both CNR and BRISQUE after incorporating self-training and $\mathcal{L}_s$. As shown in Fig. 2(g), background noise is suppressed after self-training. From Fig. 2(h), the vascular information in the ROI region of the B-scan images becomes increasingly distinct with our en face enhancement loss. After adaptation, our method achieves a denoising performance comparable to that of the source domain. These improvements demonstrate the superiority of our approach in addressing the domain gap and enhancing image quality.

En face enhancement: For en face images, we directly average and stack B-scan images along the axial direction for evaluation, followed by Min-Max normalization of the resulting stacked en face images. While $\mathcal{L}_s$ primarily constrains the B-scan, the improvement in en face images mainly relies on $\mathcal{L}_e$. With the introduction of the en face enhancement loss, our method achieves strong quantitative performance, with an entropy of 4.21 and a vessel contrast of 87.4. In Fig. 3(h), our method has better overall contrast and vascular structures than other methods. The results demonstrate the capability of our method in enhancing en face images.

3.3 Comparison with Other Methods

We compare classical OCTA imaging methods, including OCTARA [26], OMAG [29] and i-OMAG, as well as deep learning methods proposed by Li *et al.* [16] and Jiang *et al.* [11]. i-OMAG is the improved version of OMAG by utilizing

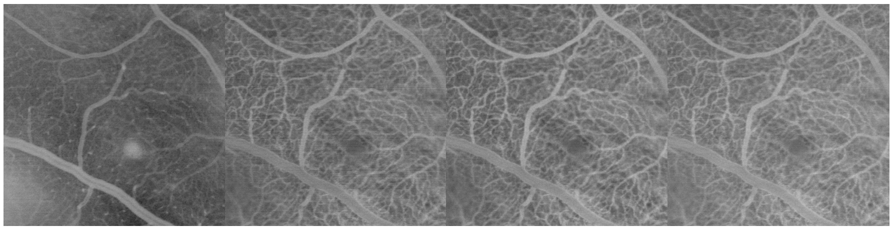

(a) OCTARA [26] (b) OMAG [29] (c) i-OMAG (d) Li *et al.* [16]

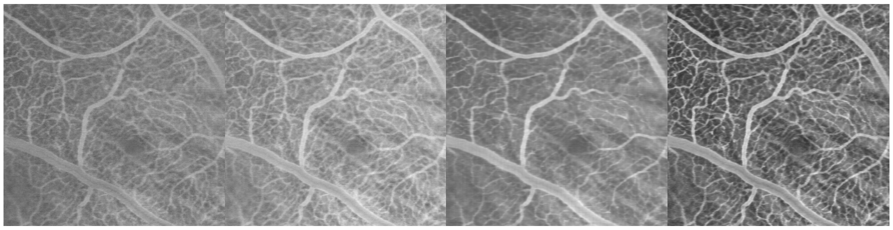

(e) Jiang *et al.* [11] (f) w/o $\mathcal{L}_s$ & $\mathcal{L}_e$ (g) w/o $\mathcal{L}_e$ (h) Ours

Fig. 3: OCTA en face images of monkey.

adjacent positions (refer to Section 2.1). The deep learning methods are trained on the target domain, and initialized with the source domain weights.

Quantitative results are presented in Table 3, while visual samples in B-scan and en face are shown in Fig. 2 and Fig. 3 respectively. Our method achieves the best quantitative scores for both monkey and human datasets. For B-scan images, our method outperforms the second-best approach by 53.1% and 65.0% in CNR and BRISQUE respectively in human subjects. The results of i-OMAG perform better than the original OMAG in B-scans, which indicates the effectiveness of utilizing adjacent positions. It is worth noting that our baseline model (w/o $\mathcal{L}_s$ & $\mathcal{L}_e$) achieves a CNR of 14.8 and a BRISQUE of 45.3 on monkey OCTA (see Table 2), outperforming other methods. Although other deep learning methods also load the weights from the source domain, poor pseudo ground truth results in detrimental optimization, which hinders effective transfer learning. For en face images, while other methods do not consider en face enhancement, our method achieves significant improvements, as shown in Fig. 3.

For full-reference evaluation, we have another machine with a different setup that can conduct 1000 overlapping scans in 2D mode for monkey. We use first 3 scans as input and synthesize the ground truth using averaging from 1000 scans for 2D imaging in this machine. Our method, without the en face enhancement loss (not applicable for 2D), applies to 234 different locations (26 different monkey eyes) and achieves a PSNR of 31.6933 and SSIM of 0.7134, surpassing OMAG, which achieves a PSNR of 24.5673 and an SSIM of 0.4759.

Both numerical and visual results demonstrate the enhancement capability of our method and its effectiveness in preserving en face vascular information. Our method has advantages in transferring learning from high-quality data, especially in scenarios where the target domain has high noise intensity. Furthermore, our method surpasses the performance boundaries of classical methods and other fully supervised methods by leveraging high-quality weights and self-supervised adaptation.

4 Conclusion

This paper introduces a cross-domain OCTA imaging algorithm that achieves B-scan denoising and en face enhancement through a self-training framework. The proposed method demonstrates robust cross-domain enhancement capabilities, surpassing the performances of fully supervised OCTA algorithms. It performs effectively on both en face and B-scan images. Incorporating attention mechanisms among various OCTA layers during enhancement will be a key focus of our future work.

Acknowledgments. This work is supported by the Agency for Science, Technology and Research under its MTC Programmatic Fund M23L7b0021 and AI^3 Horizontal Technology Coordinating Office Grant C231118001.

Disclosure of Interests. The authors have no competing interests to declare that are relevant to the content of this article.

References

1. Bernucci, M.T., Merkle, C.W., Srinivasan, V.J.: Investigation of artifacts in retinal and choroidal OCT angiography with a contrast agent. Biomedical optics express **9**(3), 1020–1040 (2018)
2. Cai, Z., Ravichandran, A., Maji, S., Fowlkes, C., Tu, Z., Soatto, S.: Exponential moving average normalization for self-supervised and semi-supervised learning. In: Proceedings of the IEEE/CVF Conference on Computer Vision and Pattern Recognition. pp. 194–203 (2021)
3. Chen, C.L., Wang, R.K.: Optical coherence tomography based angiography. Biomedical optics express **8**(2), 1056–1082 (2017)
4. Cheng, J., Tao, D., Quan, Y., Wong, D.W.K., Cheung, G.C.M., Akiba, M., Liu, J.: Speckle reduction in 3D optical coherence tomography of retina by A-scan reconstruction. IEEE Transactions on Medical Imaging **35**(10), 2270–2279 (2016)
5. Cuenca, N., Ortuno-Lizaran, I., Sanchez-Saez, X., Kutsyr, O., Albertos-Arranz, H., Fernandez-Sanchez, L., Martinez-Gil, N., Noailles, A., López-Garrido, J.A., Lopez-Galvez, M., et al.: Interpretation of OCT and OCTA images from a histological approach: clinical and experimental implications. Progress in retinal and eye research **77**, 100828 (2020)
6. Enfield, J., Jonathan, E., Leahy, M.: In vivo imaging of the microcirculation of the volar forearm using correlation mapping optical coherence tomography (cmOCT). Biomedical optics express **2**(5), 1184–1193 (2011)
7. Guizar-Sicairos, M., Thurman, S.T., Fienup, J.R.: Efficient subpixel image registration algorithms. Optics letters **33**(2), 156–158 (2008)

8. He, K., Sun, J., Tang, X.: Single image haze removal using dark channel prior. IEEE transactions on pattern analysis and machine intelligence **33**(12), 2341–2353 (2010)
9. Hu, Z., Nittala, M.G., Sadda, S.: Comparison of retinal layer intensity profiles from different OCT devices. Ophthalmic Surg Lasers Imaging Retina **44**(6 Suppl), S5–10 (2013)
10. Huang, K., Su, N., Tao, Y., Li, M., Ma, X., Ji, Z., Yuan, S., Chen, Q.: Cross-device OCTA generation by patch-based 3D multi-scale feature adaption. IEEE Transactions on Emerging Topics in Computational Intelligence (2023)
11. Jiang, Z., Huang, Z., Qiu, B., Meng, X., You, Y., Liu, X., Geng, M., Liu, G., Zhou, C., Yang, K., et al.: Weakly supervised deep learning-based optical coherence tomography angiography. IEEE Transactions on Medical Imaging **40**(2), 688–698 (2020)
12. Jiang, Z., Huang, Z., You, Y., Geng, M., Meng, X., Qiu, B., Zhu, L., Gao, M., Wang, J., Zhou, C., et al.: Rethinking the neighborhood information for deep learning-based optical coherence tomography angiography. Medical Physics **49**(6), 3705–3716 (2022)
13. Lains, I., Wang, J.C., Cui, Y., Katz, R., Vingopoulos, F., Staurenghi, G., Vavvas, D.G., Miller, J.W., Miller, J.B.: Retinal applications of swept source optical coherence tomography (OCT) and optical coherence tomography angiography (OCTA). Progress in retinal and eye research **84**, 100951 (2021)
14. Lehtinen, J., Munkberg, J., Hasselgren, J., Laine, S., Karras, T., Aittala, M., Aila, T.: Noise2Noise: Learning image restoration without clean data. arXiv preprint arXiv:1803.04189 (2018)
15. Li, M., Huang, K., Xu, Q., Yang, J., Zhang, Y., Ji, Z., Xie, K., Yuan, S., Liu, Q., Chen, Q.: OCTA-500: a retinal dataset for optical coherence tomography angiography study. Medical image analysis **93**, 103092 (2024)
16. Li, P.L., O'Neil, C., Saberi, S., Sinder, K., Wang, K., Tan, B., Hosseinaee, Z., Bizhevat, K., Lakshminarayanan, V.: Deep learning algorithm for generating optical coherence tomography angiography (OCTA) maps of the retinal vasculature. In: Applications of Machine Learning 2020. vol. 11511, pp. 39–49. SPIE (2020)
17. Lin, Z., Zhang, Q., Lan, G., Xu, J., Qin, J., An, L., Huang, Y.: Deep learning for motion artifact-suppressed OCTA image generation from both repeated and adjacent OCT scans. Mathematics **12**(3), 446 (2024)
18. Liu, G., Jia, Y., Pechauer, A.D., Chandwani, R., Huang, D.: Split-spectrum phase-gradient optical coherence tomography angiography. Biomedical Optics Express **7**(8), 2943–2954 (2016)
19. Liu, X., Huang, Z., Wang, Z., Wen, C., Jiang, Z., Yu, Z., Liu, J., Liu, G., Huang, X., Maier, A., et al.: A deep learning based pipeline for optical coherence tomography angiography. Journal of Biophotonics **12**(10), e201900008 (2019)
20. Ma, Y., Yan, Q., Liu, Y., Liu, J., Zhang, J., Zhao, Y.: StruNet: Perceptual and low-rank regularized transformer for medical image denoising. Medical Physics **50**(12), 7654–7669 (2023)
21. Massey Jr, F.J.: The Kolmogorov-Smirnov test for goodness of fit. Journal of the American statistical Association **46**(253), 68–78 (1951)
22. Mittal, A., Moorthy, A.K., Bovik, A.C.: No-reference image quality assessment in the spatial domain. IEEE Transactions on image processing **21**(12), 4695–4708 (2012)
23. Myung, I.J.: Tutorial on maximum likelihood estimation. Journal of mathematical Psychology **47**(1), 90–100 (2003)

24. Rocholz, R., Corvi, F., Weichsel, J., Schmidt, S., Staurenghi, G.: OCT angiography (OCTA) in retinal diagnostics. High resolution imaging in microscopy and ophthalmology: new frontiers in biomedical optics pp. 135–160 (2019)
25. Sohn, K., Berthelot, D., Carlini, N., Zhang, Z., Zhang, H., Raffel, C.A., Cubuk, E.D., Kurakin, A., Li, C.L.: Fixmatch: Simplifying semi-supervised learning with consistency and confidence. Advances in neural information processing systems **33**, 596–608 (2020)
26. Stanga, P.E., Tsamis, E., Papayannis, A., Stringa, F., Cole, T., Jalil, A.: Swept-source optical coherence tomography angio™ (Topcon Corp, Japan): technology review. OCT Angiography in Retinal and Macular Diseases **56**, 13–17 (2016)
27. Tsai, D.Y., Lee, Y., Matsuyama, E.: Information entropy measure for evaluation of image quality. Journal of digital imaging **21**, 338–347 (2008)
28. Uji, A., Balasubramanian, S., Lei, J., Baghdasaryan, E., Al-Sheikh, M., Borrelli, E., Sadda, S.R.: Multiple enface image averaging for enhanced optical coherence tomography angiography imaging. Acta ophthalmologica **96**(7), e820–e827 (2018)
29. Wang, R.K., Jacques, S.L., Ma, Z., Hurst, S., Hanson, S.R., Gruber, A.: Three dimensional optical angiography. Optics express **15**(7), 4083–4097 (2007)
30. Welvaert, M., Rosseel, Y.: On the definition of signal-to-noise ratio and contrast-to-noise ratio for fMRI data. PloS one **8**(11), e77089 (2013)
31. Xu, Y., Xu, X., Jin, L., Gao, S., Goh, R.S.M., Ting, D.S.W., Liu, Y.: Partially-supervised learning for vessel segmentation in ocular images. In: MICCAI 2021. pp. 271–281. Springer International Publishing, Cham (2021)
32. Yang, B., Cao, L., Zhao, H., Li, H., Liu, H., Wang, N.: Adaptive enhancement of cataractous retinal images for contrast standardization. Medical & Biological Engineering & Computing **62**(2), 357–369 (2024)
33. Yang, D., Ran, A.R., Nguyen, T.X., Lin, T.P., Chen, H., Lai, T.Y., Tham, C.C., Cheung, C.Y.: Deep learning in optical coherence tomography angiography: Current progress, challenges, and future directions. Diagnostics **13**(2), 326 (2023)